ACS OMEGA

http://pubs.acs.org/journal/acsodf

Article

Pseudocapacitive Deionization of Saltwater by Mn_3O_4@C/Activated Carbon

Po-An Chen, Shou-Heng Liu, and H. Paul Wang*

Cite This: *ACS Omega* 2023, 8, 13315−13322

Read Online

ACCESS | Metrics & More | Article Recommendations

ABSTRACT: Capacitive deionization (CDI), a m ethod with notable advantages of relatively low energy consumption and environmental friendliness, has been widely used in desalination of saltwater. However, due to the weak electrical double-layer electrosorption of ions from water, CDI has suffered from low throughput capacity that may limit its commercial applications. Thus, it is of importance to develop a high-efficiency and engineering-feasible CDI process. Manganese and cobalt and their oxides, being faradic materials, have a relatively high pseudocapacitance, which can cause an increase of positive and negative charges on opposing electrodes. However, their low conductivity properties limit their electrochemical applications. Pseudocapacitive Mn_3O_4 nanoparticles encapsulated within a conducting carbon shell (Mn_3O_4@C) were prepared to enhance charge transfer and capacitance for CDI. Desalination performances of the Mn_3O_4@C (5−15 wt %) core−shell nanoparticles on activated carbon (AC) (Mn_3O_4@C/AC) serving as CDI electrodes have thus been investigated. The pseudocapacitive Mn_3O_4@C/AC electrodes with relatively low diffusion resistances have much greater capacitance (240−1300 F/g) than the pristine AC electrode (120 F/g). *In situ* synchrotron X-ray absorption near-edge structure spectra of the Mn_3O_4@C/AC electrodes during CDI (under 1.2 and −1.2 V for electrosorption and regeneration, respectively) demonstrate that reversible faradic redox reactions $(Mn_3O_4)@C \underset{-e^-}{\overset{+e^-}{\rightleftarrows}} (Mn_2O_3{+}MnO)@C$ cause more negative charges on the negative electrode and more positive charges on the positive electrode. Consequently, the pseudocapacitive electrodes for CDI of saltwater ([NaCl] = 1000 ppm) show much better desalination performances with a high optimized salt removal (600 mg/g·day), electrosorption efficiency (48%), and electrosorption capacity (EC) (25 mg/g) than the AC electrodes (288 mg/g·day, 23%, and 12 mg/g, respectively). The Mn_3O_4@C/AC electrode has a maximum EC of 29 mg/g for CDI under +1.2 V. Also, the Mn_3O_4@C/AC electrodes have much higher pseudocapacitive electrosorption rate constants (0.0049−0.0087 h^{-1}) than the AC electrode (0.0016 h^{-1}). This work demonstrates the feasibility of high-efficiency CDI of saltwater for water recycling and reuse using the low-cost and easily fabricated pseudocapacitive Mn_3O_4@C/AC electrodes.

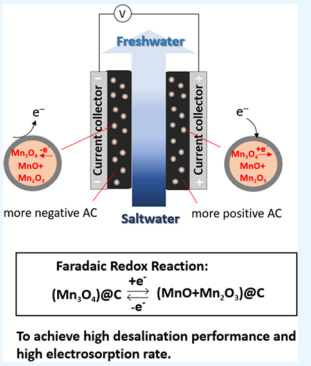

1. INTRODUCTION

In response to the shortage and uneven water distribution of freshwater, developing effective methods for desalination of saltwater to freshwater is of increasing importance.[1−3] Attributable to the environmental friendliness and relatively low energy consumption, capacitive deionization (CDI) using carbon electrodes has been widely studied for the desalination of saltwater.[4−6] The CDI cell is generally comprised of two conductive electrodes coated with high surface area carbon materials such as activated carbon (AC), carbon nanotubes, carbon fibers, and graphene.[7−10] Under applied voltages (0.6−1.5 V), electrical double layers (EDLs) are formed on the surfaces of the carbon electrodes for electrosorption of opposite ions.[11,12] Ions that are captured by EDLs depend on the capacitance and pore structure of the carbon materials.[13−16] The typical CDI processes based on the weak electrosorption on EDLs have, however, common drawbacks of low throughput capacity and electrosorption rates that may limit their commercial applications.[17]

Additional faradic electrosorption through redox reactions can be obtained by incorporating pseudocapacitive materials such as transition metal/metal oxides and conducting polymers in the carbon electrodes.[18−20] Transition metal oxides with high pseudocapacitance have been used to provide (or remove) extra charges through faradic reactions near the EDLs. For example, expensive ruthenium having a very high specific capacitance (about 1300 F/g) was used in high-

Received: February 1, 2023
Accepted: March 17, 2023
Published: March 28, 2023

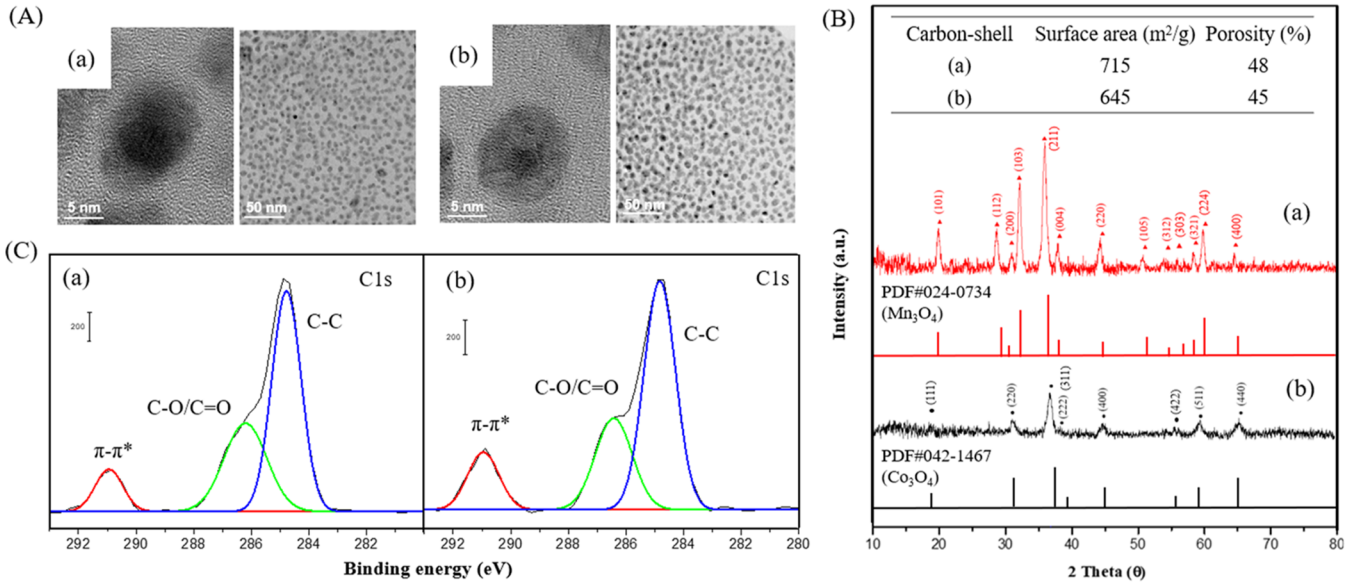

Figure 1. (A) TEM images at 3,000,000 and 300,000 magnifications, (B) XRD patterns with corresponding PDF standard patterns and (C) deconvoluted C 1s XPS spectra of the pseudocapacitive (a) Mn_3O_4@C and (b) Co_3O_4@C core−shell nanoparticles. The specific surface areas and porosities of the carbon shell nanoparticles are also shown in the inset.

performance supercapacitors.[21,22] Thus, CDI electrodes having high capacitances can highly promote their desalination performances.

Manganese oxides with advantages of low cost, low toxicity, easy synthesis, and environmental friendliness have noteworthy pseudocapacitive activity.[23−25] Cobalt oxides also gain prominence due to their high theoretical specific capacitance.[26] However, they suffer from relatively low conductivity for CDI electrode materials, which can be improved by dispersion in carbon nanofoam, mesoporous carbon, graphite, nanotube carbon, and graphene.[27−30] For example, the capacitance enhancement of the Co_3O_4/rGO electrode (from 44 to 472 F/g) is mainly associated with the pseudocapacitance of the electrochemically active Co_3O_4 ($Co_3O_4 + 4OH^- \rightarrow 3CoO_2 + 2H_2O + 3e^-$).[31] Mn_3O_4 has many advantages such as multi-oxidation state and high theoretical capacity (1400 F/g).[32] An rGO@Mn_3O_4 electrode has multivalent redox states (+2, +3, and +4) and extended action potential of 1.2 V (compared to Ag/AgCl) through the oxidation of Mn^{4+} to Mn^{7+}.[33] Mn^{3+} in Mn_3O_4@NPC in the anodic charging step can be oxidized to Mn^{4+}. In the subsequent cathodic scan, most of the Mn^{4+} ions are reduced and a structural reconstruction from Mn_3O_4 to δ-MnO_2 takes place on the electrode surface.[34] Mn_3O_4@N, P-doped carbon (Mn_3O_4@NPC) has higher EDL capacitance and pseudocapacitance than Mn_3O_4 and carbonized chitosan by 50% and 124%, respectively.[34] In separate experiments, we also found that the porous carbon shells of Ag@C and (Cu-Ag)@C core−shell nanoparticles with desired conductivities accounted for their relatively high electrosorption rates and desalination performances.[7,35]

In this work, new pseudocapacitive core−shell nanoparticle, i.e., Mn_3O_4 and Co_3O_4 (for comparison) encapsulated within a conductive carbon shell (Mn_3O_4@C and Co_3O_4@C), dispersed AC (Mn_3O_4@C/AC and Co_3O_4@C/AC) electrodes were prepared for CDI. Electrochemical properties of the Mn_3O_4@C/AC and Co_3O_4@C/AC electrodes were investigated by cyclic voltammetry (CV) and electrochemical impedance spectroscopy (EIS). The chemical structure of the Mn_3O_4@C/AC and Co_3O_4@C/AC electrodes was also studied by *in situ* synchrotron X-ray absorption near-edge structure (XANES) for a better understanding of the faradic redox reactions during CDI.

2. MATERIALS AND METHODS

The Mn_3O_4@C and Co_3O_4@C core−shell nanoparticles were prepared by the carbonization method.[36] Briefly, Mn(II) nitrate tetrahydrate ($Mn(NO_3)_2{\cdot}4H_2O$) (Sigma-Aldrich, 98%) [or Co(II) nitrate hexahydrate ($Co(NO_3)_2{\cdot}6H_2O$) (Alfa Aesar, 98%)] was chelated with β-cyclodextrin (β-CD) (Sigma-Aldrich) in deionized water (200 mL) at the C-to-Mn (or Co) mole ratio of 6. The complex was stirred at 298 K for 1 h, dried at 333 K for 16 h, and carbonized at 673 K for 4 h under flowing high-purity nitrogen gas (100 mL/min) to form the Mn_3O_4@C (or Co_3O_4@C) core−shell nanoparticles. The as-synthesized core−shell nanoparticles (10 wt %) were dispersed in activated carbon (AC) (Goldstar Carbon Tech Inc.) to form Mn_3O_4@C/AC and Co_3O_4@C/AC. After being mixed with polyvinylidene fluoride (PVdF) (Sigma-Aldrich) (10 wt %) and N-methyl-2-pyrrolidone (NMP) (Sigma-Aldrich) (20 wt %) at 298 K for 3 h, they were coated on graphite electrodes (2.5 × 2.5 cm^2). The Mn_3O_4@C/AC and Co_3O_4@C/AC electrodes were then dried at 353 K for 6 h for CDI experiments.

Images of the Mn_3O_4@C and Co_3O_4@C nanoparticles were determined by high-resolution analytical transmission electron microscopy (TEM) (JEOL, JEM-3010 and JEOL, JEM-2100F) and scanning electron microscopy (SEM) (JEOL, JSM-6700) (at the operation voltages of 200 and 10 keV). The chemical structure of the core−shell nanoparticles was determined by X-ray diffraction (XRD) (BRUKER, D8 Advance) with Cu Kα radiation between 10° to 80° (2θ) at a scan rate of 5°/min under the working voltage of 40 kV (40 mA). Their surface chemical structures were also determined by X-ray photoelectron spectroscopy (XPS, PHI500). Electrochemical properties of the Mn_3O_4@C/AC and Co_3O_4@C/AC electrodes were studied by cyclic voltammetry (CV) and electrochemical

https://doi.org/10.1021/acsomega.3c00673
ACS Omega 2023, 8, 13315−13322

impedance spectroscopy (EIS) on a three-electrode system including the counter and reference electrodes. The specific capacitance (C) (F/g) was determined by $C = S/2vm$ (S: area of cyclic voltammograms (V.A); v and m: scan rate and amount (g) of electrode materials coated on the graphite sheets, respectively).

Real-time chemical structure data of manganese and cobalt in the Mn_3O_4@C/AC and Co_3O_4@C/AC electrodes were studied by *in situ* synchrotron X-ray absorption near-edge structure (XANES) spectroscopy on the Wiggler beamline at the Taiwan National Synchrotron Radiation Research Center. The XANES spectra of manganese and cobalt in the energy range of 7700−7800 and 6500−6700 eV, respectively, extend to an energy of 50 eV above the edge. During *in situ* XANES studies, the synchrotron X-ray passed through the space between the electrode pair for monitoring the structural changes of the Mn_3O_4@C/AC and Co_3O_4@C/AC electrodes. The XANES spectra were analyzed by principal-component and least-squares fittings.

The desalination performance experiments were carried out with a parallel electrode (2.5 × 2.5 cm^2) pair using simulated saltwater samples ([NaCl] = 100 and 1000 ppm) under +1.2 and 0 V for electrosorption and regeneration, respectively. The desalination performance (related to electrosorption capacity (EC), optimized salt removal (OSR), and recycling performance) of CDI using the pseudocapacitive electrodes was determined by monitoring the electrical conductivity changes (normalized to concentration). The EC (mg/g) data were determined by EC = ΔC·V/W (ΔC: concentration difference (mg/L); V: saltwater volume (L), and W: composite weight (g)). The OSR (mg/g·day) represents the amount (mg) of salt removed per gram of the pseudocapacitive electrode materials during a predetermined operational time (day).

3. RESULTS AND DISCUSSION

The TEM images of the pseudocapacitive Mn_3O_4@C and Co_3O_4@C core−shell nanoparticles are shown in Figure 1A. The core−shell nanoparticles are well dispersed in AC. The core Mn_3O_4 and Co_3O_4 having nanoparticle size of 7−9 nm

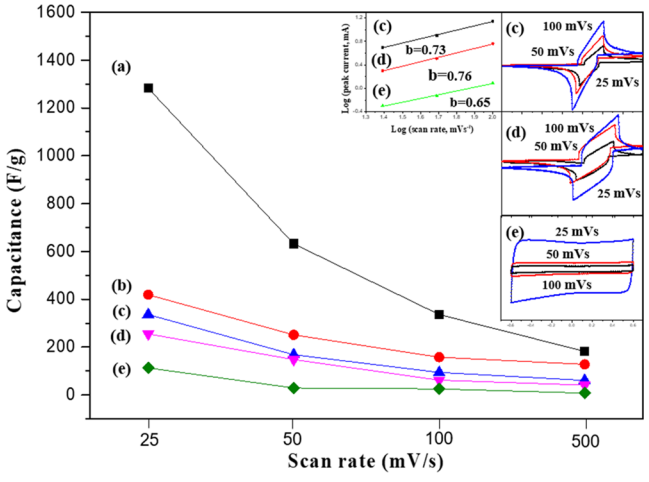

Figure 2. Cyclic voltammograms, capacitances, and plots of log(scan rate) versus log(peak current) of the (a) Mn_3O_4@C/AC, (b) Co_3O_4@C/AC, (c) Mn_3O_4@C, (d) Co_3O_4@C, and (e) AC electrodes at sweep rates of 25, 50, and 100 mV/s in NaCl (1.0 M) solution.

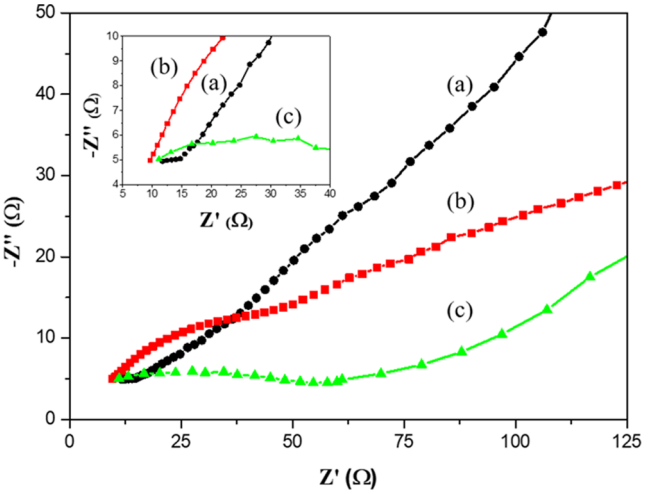

Figure 3. Electrochemical impedance spectra (EIS) of the (a) Mn_3O_4@C/AC, (b) Co_3O_4@C/AC, and (c) AC electrodes. The EIS spectra in the high-frequency region are also shown in the inset.

are encapsulated within carbon shells (thickness: 3−5 nm). The XRD patterns of the Mn_3O_4@C and Co_3O_4@C nanoparticles and their corresponding PDF standard patterns[37,38] are shown in Figure 1B. Characteristic diffraction peaks of the Co_3O_4@C nanoparticles are observed at 2θ = 31.3° (220), 36.9° (311), 38.5° (222), 44.8° (400), 55.6° (422), 59.3° (440), 65.2° (511), and 77.3° (533), suggesting the existence of Co_3O_4. The diffraction peaks at 17.9, 28.8, 30.1, 32.3, 36.1, 38, 44.5, 50.7, 54.4, 56.1, 58.3, 59.8, and 64.7° can be assigned to the Mn_3O_4 (101), (112), (200), (103), (211), (004), (220), (105), (312), (303), (321), (224), and (400) planes, respectively. The weak and broadened bands at 10−15° may be related to the amorphous carbon shell. Specific surface areas and porosities of the pseudocapacitive Mn_3O_4@C and Co_3O_4@C core−shell nanoparticles have also been investigated and are shown in the inset of Figure 1B. The carbon shells in the Mn_3O_4@C and Co_3O_4@C core−shell nanoparticles have specific surface areas of 715 and 645 m^2/g, respectively. Minimal differences in porosities between the Mn_3O_4@C (48%), Co_3O_4@C (45%), Mn_3O_4@C/AC (52%), and Co_3O_4@C/AC (50%) electrodes have also been observed (Figure 1B). It seems that the effects of porosities of the core−shell nanoparticles could not be a major contributing factor for the desalination performance.

The chemical structure of the carbon shell in the Mn_3O_4@C and Co_3O_4@C core−shell nanoparticles has been studied by C 1s XPS spectra. Figure 1C shows that the deconvoluted C 1s XPS spectra of the core−shell nanoparticles have three peaks at 291, 287, and 285 eV which are associated with $\pi-\pi^*$ interactions, C-O and/or C═O (C-O/C═O), and C-C, respectively.[39−42] The carbon shell of the core−shell nanoparticles may have $\pi-\pi^*$ interactions with the core Mn_3O_4 and Co_3O_4 to yield the C-O/C═O species.[39,40] During pseudocapacitive CDI, for example, under 1.2 V, electron transfers between water and the carbon shell may also involve redox reactions to form the C-O or C═O species. These electron transfer routes enable the carbon shell of the Mn_3O_4@C and Co_3O_4@C core−shell nanoparticles to serve as an electron reservoir in the pseudocapacitive CDI process.[41−43]

Cyclic voltammetry (CV) curves and capacitances of the AC, Mn_3O_4@C/AC, Co_3O_4@C/AC, Co_3O_4@C, and Mn_3O_4@C electrodes are shown in Figure 2. Capacitances of

https://doi.org/10.1021/acsomega.3c00673
ACS Omega 2023, 8, 13315−13322

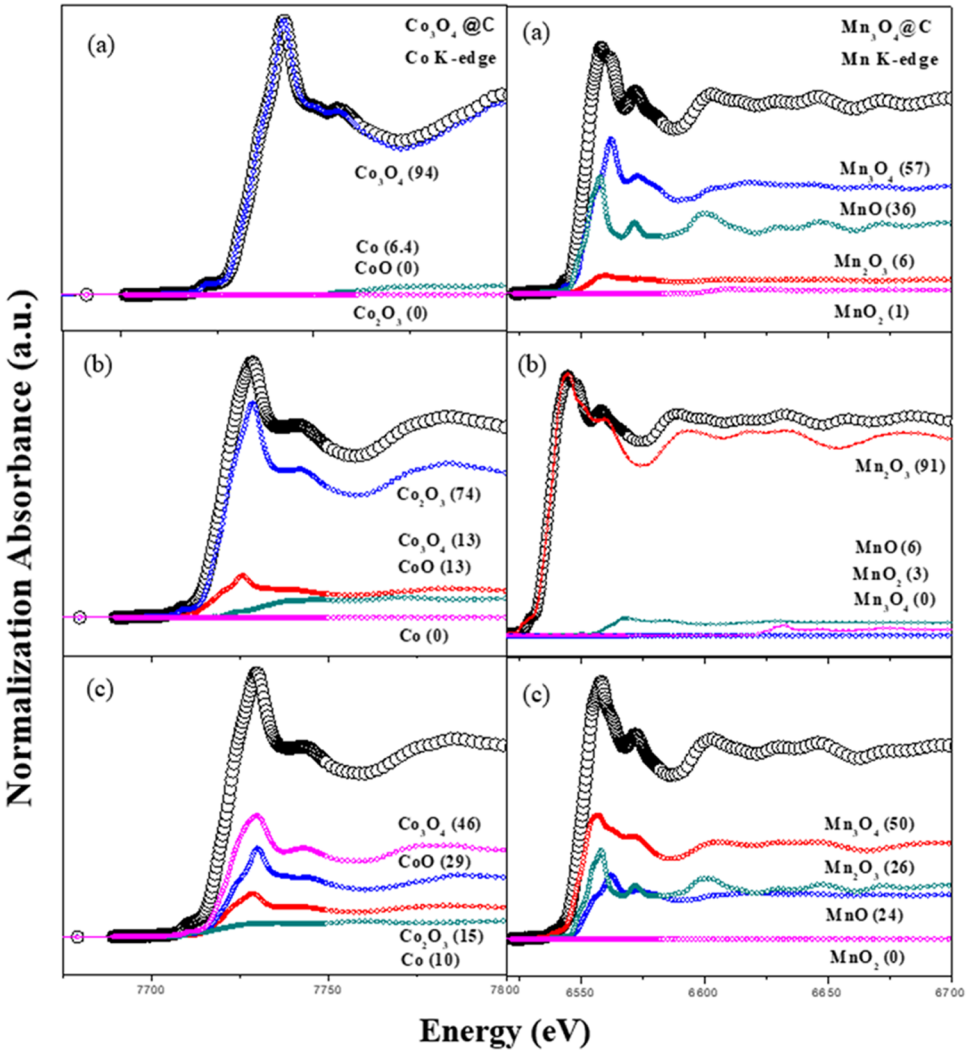

Figure 4. Component-fitted XANES spectra of the Co_3O_4@C/AC and Mn_3O_4@C/AC electrodes under (a) 0, (b) +1.2 (for electrosorption), and (c) −1.2 V (for desorption (regeneration)) during CDI.

the Mn_3O_4@C and Co_3O_4@C electrodes with non-rectangular shapes of the CV curves are 370 and 251 F/g, respectively. Intensities of the pseudocapacitive Mn_3O_4@C and Co_3O_4@C electrodes increase with a similar shape as the scan rate is increased from 25 to 500 mV/s, suggesting the electrochemical stability of the pseudocapacitive electrodes. Moreover, the redox reactions are reversible at scan rates between 25 and 500 mV/s, signifying that the pseudocapacitance of the oxides is associated with the faradic redox reactions. It should be noted that the AC electrode has a much less specific capacitance (120 F/g) than the Mn_3O_4@C/AC and Co_3O_4@C/AC electrodes (1300 and 420 F/g, respectively) at the scan rate of 25 mV/s. The peak current intensity (i) has a certain relationship with the scanning rate (v) (log(i) = log(a) + blog(v)).[44] The *b* value generated by the slope can be used to determine the desalination control mechanism of the electrode. Theoretically, a slope value of 1.0 suggests that the electrochemical reaction occurs on the surface of the electrode, while *a* value of 0.5 indicates that the current is controlled by a semi-infinite diffusion-controlled process.[45] As shown in Figure 2, the Mn_3O_4@C, Co_3O_4@C, and AC electrodes have *b* values of 0.73, 0.76, and 0.65, respectively, suggesting the high possibility of more capacitive and less diffusion-controlled contributions to desalination performance by the pseudocapacitive core−shell nanoparticles.

Resistivities of the pseudocapacitive Mn_3O_4@C/AC and Co_3O_4@C/AC electrodes were determined by electrochemical impedance spectroscopy (EIS) at a frequency range between 0.01 and 100 kHz in a NaCl (1 M) aqueous solution. In Figure 3, a nearly straight line is observed in the Nyquist plots at the low-frequency region for the Mn_3O_4@C/AC electrode, suggesting a fast diffusion and electrosorption of ions to the electrode, which may be associated with the Warburg impedance that may reduce the diffusion resistance.[46] In the high-frequency region, the Nyquist plots for the Mn_3O_4@C/AC electrode exhibit a relatively low electrical resistance and high electron transport as this electrode has a smaller arc diameter than the Co_3O_4@C/AC and AC electrodes.

By *in situ* XANES spectroscopy, the molecular-scale data for redox reactions of the pseudocapacitive electrodes during CDI have been determined. Component-fitted XANES spectra of the Mn_3O_4@C/AC electrode under 0, +1.2, and −1.2 V during CDI are shown in Figure 4. The *in situ* XANES spectra of the Mn_3O_4@C/AC electrode show the existence of Mn_3O_4 (57%), Mn_2O_3 (6%), and MnO (36%). In the CDI process under +1.2 V, more negative and positive charges on the negative and

https://doi.org/10.1021/acsomega.3c00673
ACS Omega 2023, 8, 13315−13322

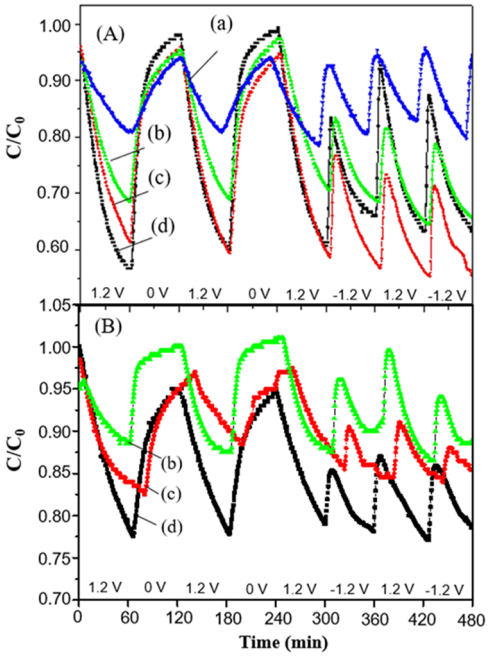

Figure 5. Electrosorption of saltwater ([NaCl] = 100 ppm) by the (A) Mn_3O_4@C/AC and (B) Co_3O_4@C/AC electrodes containing the core−shell nanoparticles ((a) 0, (b) 5, (c) 10, and (d) 15 wt %) during CDI under +1.2 V (electrosorption), 0 V (desorption for regeneration), and −1.2 V (desorption for regeneration) for 6 h.

Table 1. Pseudocapacitive Electrosorption Rate Constants (k) (the Pseudo-First-Order Reaction) for CDI of a Simulated Saltwater Sample ([NaCl] = 100 ppm) under +1.2 V[a]

electrodes	Mn_3O_4@C (wt %)	k
Mn_3O_4@C/AC	5	0.0049
Mn_3O_4@C/AC	10	0.0066
Mn_3O_4@C/AC	15	0.0087
AC	0	0.0016

[a] ($R^2 > 0.99$).

Table 2. Electrosorption Efficiency (EE) and Electrosorption Capacity (EC) of Pseudocapacitive Electrodes for CDI of Saltwater under 1.2 V

electrode materials	EE (%)	EC (mg/g)	ref
RuO_2-AC	36	11	19
Mn_3O_4 nanowires	44	23	48
$MnFe_2O_4$/porous rGO	17	8.9	49
MnO_2-rGO/rGO	26	21	50
Mn_3O_4@C/AC	48	25	this work
Co_3O_4@C/AC	32	17	this work

positive electrodes, respectively, are contributed by the faradic redox reactions $(Mn_3O_4)@C \underset{e^-}{\overset{+e^-}{\rightleftharpoons}} (Mn_2O_3(91\%) + MnO(6\%))@C$. Also, the Mn_3O_4@C electrode has a high pseudocapacitance (370 F/g) with an enlarged redox potential window.[47] During desorption for regeneration under −1.2 V, the reversible faradic redox reactions in a similar but reverse way can also promote the release of ions from electrodes. Furthermore, the carbon shell of the core−shell nanoparticle serves as an electron reservoir to rapidly transfer the faradic redox electrons to or from the AC

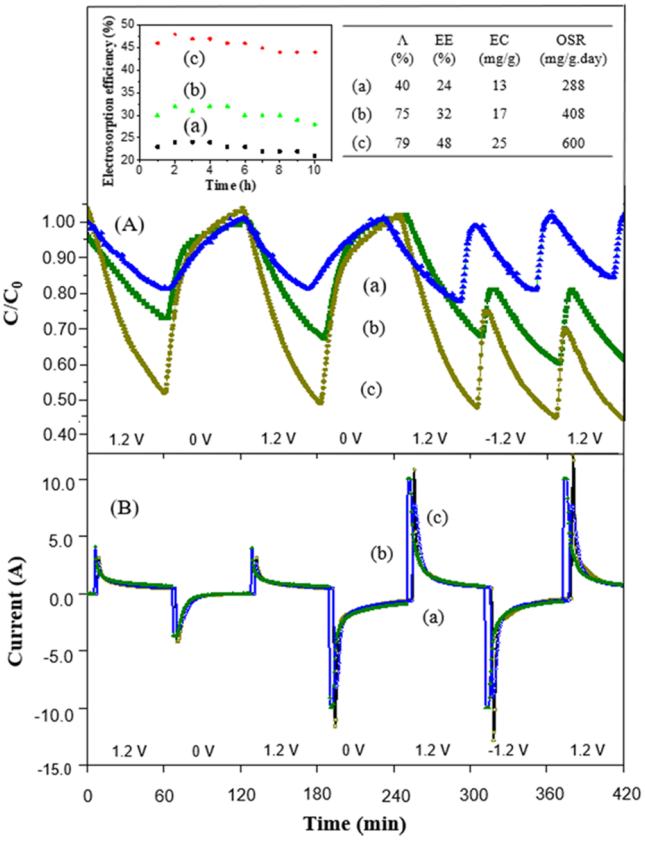

Figure 6. (A) Electrosorption and (B) current profiles of ions during pseudocapacitive CDI of saltwater ([NaCl] = 1000 ppm) by the (a) AC, (b) Co_3O_4@C/AC (Co_3O_4@C: 15 wt %), and (c) Mn_3O_4@C/AC (Mn_3O_4@C: 15 wt %) electrodes. Their charge efficiencies (Λ), electrosorption efficiency (EE), electrosorption capacity (EC), optimized salt removal (OSR), and recycling performance for 10 h are shown in the insets.

electrodes. The Co_3O_4@C/AC behaves similarly as well, i.e., the reversible faradic redox reactions $(Co_3O_4)@C \underset{e^-}{\overset{+e^-}{\rightleftharpoons}} (Co_2O_3(74\%) + CoO(13\%))@C$ during CDI under +1.2 and −1.2 V for electrosorption and regeneration, respectively. It is demonstrated that the pseudocapacitive M_3O_4@C/AC and Co_3O_4@C/AC electrodes involving reversible faradic redox reactions in the CDI processes have relatively high electrosorption and regeneration efficiencies.

Figure 5A shows the electrosorption kinetics of the Mn_3O_4@C/AC and AC electrodes. Their reaction rate constants are well-fitted to the experimental data ($R^2 > 0.99$) using the pseudo-first-order kinetic model (Table 1). The AC electrode has a rate constant (k) of 0.0016 h^{-1}, while the pseudocapacitive Mn_3O_4@C/AC electrodes have much higher k (0.0049−0.0087 h^{-1}). The enhanced electrosorption efficiency of the Mn_3O_4@C/AC electrodes is contributed by their high pseudocapacitance causing reversible faradic redox reactions.

Desalination performances associated with optimized salt removal (OSR) (mg/g·day), electrosorption efficiency (EE) (%), and electrosorption capacity (EC) (mg/g) of the pseudocapacitive electrodes for CDI of simulated saltwater samples ([NaCl] = 100 and 1000 ppm) have been examined. Electrosorption (+1.2 V) and desorption for regeneration (0

https://doi.org/10.1021/acsomega.3c00673
ACS Omega 2023, 8, 13315−13322

and −1.2 V) of the AC and Mn_3O_4@/AC electrodes for CDI of saltwater ([NaCl] = 100 ppm) are shown in the inset of Figure 5A. The Mn_3O_4@C/AC electrodes have relatively high EEs under the reversed voltage (−1.2 V) for desorption (regeneration). In the first electrosorption cycle, the EEs of the Mn_3O_4@C/AC and AC electrodes are 35% and 20%, respectively, suggesting that the pseudocapacitance contributions of the Mn_3O_4@C to EE can be as high as 10%. The effect of the pseudocapacitive Co_3O_4@C nanoparticle content (5−15 wt %) in electrodes on EE is shown in Figure 5B. The EC and OSR of the Mn_3O_4@C/AC electrode for CDI of saltwater ([NaCl] = 100 ppm) are 18 mg/g and 432 mg/g·day, respectively, which are greater than those of the Co_3O_4@C/AC (14 mg/g and 336 mg/g·day) and AC electrode (10 mg/g and 240 mg/g·day). As expected, their EEs increase as more pseudocapacitive M_3O_4@C nanoparticles are added into the AC electrodes, signifying that the pseudocapacitance is essential to the desalination performance. A comparison of the EE and EC for CDI of saltwater using different pseudocapacitive electrodes is shown in Table 2. It is clear that the Mn_3O_4@C/AC electrode has comparable EE and EC with Mn_3O_4 nanowires[48] and is much better than other pseudocapacitive electrodes.

Figure 6A shows electrosorption of saltwater ([NaCl] = 1000 ppm) using the AC, Co_3O_4@C/AC, and Mn_3O_4@C/AC electrodes. The Mn_3O_4@C/AC electrode with a high EE (48%) and OSR (600 mg/g·day) has a better desalination performance than the other electrodes. In the first cycle, the EC of the Mn_3O_4@C/AC electrode can be as high as 25 mg/g. It is worth mentioning that the Mn_3O_4@C/AC and Co_3O_4@C/AC electrodes have enhanced EEs (56 and 39%) and ECs (29 and 20 mg/g) as reversed voltage (−1.2 V) is applied for desorption (regeneration). On the contrary, an insignificant effect by the reversed voltage (−1.2 V) operation is observed with the AC electrode without pseudocapacitance. The current profiles of the AC and M_3O_4@C electrodes are shown in Figure 6B with charge efficiencies between 40 and 79%. The pseudocapacitive Mn_3O_4@C/AC and Co_3O_4@C/AC electrodes exhibit relatively high charge efficiencies that can also lead to reduced energy consumption.

4. CONCLUSIONS

Pseudocapacitive Mn_3O_4@C/AC electrodes have a relatively high specific capacitance (1300 F/g) with much higher electrosorption rate constants (0.0049−0.0087 h^{-1}) than the AC electrode (0.0016 h^{-1}). *In situ* X-ray absorption near-edge structure spectra of the Co_3O_4@C/AC and Mn_3O_4@C/AC electrodes show that Co_3O_4 and Mn_3O_4 are oxidized to Co_2O_3 (74%) and Mn_2O_3 (91%), respectively, during pseudocapacitive CDI. The desalination performances with a high optimized salt removal (600 mg/g·day), electrosorption efficiency (48%), and electrosorption capacity (EC) (25 mg/g) of the pseudocapacitive electrodes for CDI of saltwater ([NaCl] = 1000 ppm) are much higher than those of the AC electrode (288 mg/g·day, 23%, and 12 mg/g, respectively). The Mn_3O_4@C/AC electrode also has a maximum EC of 29 mg/g under +1.2 for electrosorption and −1.2 V for desorption (regeneration). This work demonstrates the feasibility of the highly enhanced desalination performances for CDI of saltwater to freshwater using the low-cost and easily fabricated pseudocapacitive Mn_3O_4@C/AC electrodes.

■ ASSOCIATED CONTENT

Data Availability Statement

The data that support this study will be shared upon reasonable request to the corresponding author.

■ AUTHOR INFORMATION

Corresponding Author

H. Paul Wang − *Department of Environmental Engineering, National Cheng Kung University, Tainan 701, Taiwan;* orcid.org/0000-0001-7272-8031; Phone: +886-6275-7575; Email: wanghp@ncku.edu.tw

Authors

Po-An Chen − *Department of Environmental Engineering, National Cheng Kung University, Tainan 701, Taiwan*

Shou-Heng Liu − *Department of Environmental Engineering, National Cheng Kung University, Tainan 701, Taiwan*

Complete contact information is available at: https://pubs.acs.org/10.1021/acsomega.3c00673

Notes

The authors declare no competing financial interest.

■ ACKNOWLEDGMENTS

Financial support from the Taiwan Ministry of Science and Technology (MOST 110-2221-E-006-107-MY2, 109-2221-E-006 -042 -MY3, and 108-2221-E-006-165-MY3) and Environmental Protection Administration (10GA0008001047) is acknowledged.

■ REFERENCES

(1) Hawks, S. A.; Ramachandran, A.; Porada, S.; Campbell, P. G.; Suss, M. E.; Biesheuvel, P.; Santiago, J. G.; Stadermann, M. Performance metrics for the objective assessment of capacitive deionization systems. *Water Res.* **2019**, *152*, 126−137.

(2) Wang, H.; Yan, T.; Shen, J.; Zhang, J.; Shi, L.; Zhang, D. Efficient removal of metal ions by capacitive deionization with straw waste derived graphitic porous carbon nanosheets. *Environ. Sci.: Nano* **2020**, *7*, 317−326.

(3) Ashraf, H. M.; Al-Sobhi, S. A.; El-Naas, M. H. Mapping the desalination journal: A systematic bibliometric study over 54 years. *Desalination* **2022**, *526*, No. 115535.

(4) Chong, L.-G.; Chen, P.-A.; Huang, J.-Y.; Huang, H.-L.; Wang, H. P. Capacitive deionization of a RO brackish water by AC/graphene composite electrodes. *Chemosphere* **2018**, *191*, 296−301.

(5) Qin, M.; Deshmukh, A.; Epsztein, R.; Patel, S. K.; Owoseni, O. M.; Walker, W. S.; Elimelech, M. Comparison of energy consumption in desalination by capacitive deionization and reverse osmosis. *Desalination* **2019**, *455*, 100−114.

(6) Wang, R.; Sun, K.; Zhang, Y.; Qian, C.; Bao, W. Dimensional optimization enables high-performance capacitive deionization. *J. Mater. Chem. A* **2022**, *10*, 6414−6441.

(7) Chen, P.-A.; Cheng, H.-C.; Wang, H. P. Activated carbon recycled from bitter-tea and palm shell wastes for capacitive desalination of salt water. *J. Cleaner Prod.* **2018**, *174*, 927−932.

(8) Xu, X.; Allah, A. E.; Wang, C.; Tan, H.; Farghali, A. A.; Khedr, M. H.; Malgras, V.; Yang, T.; Yamauchi, Y. Capacitive deionization using nitrogen-doped mesostructured carbons for highly efficient brackish water desalination. *Chem. Eng. J.* **2019**, *362*, 887−896.

(9) Zhang, J.; Yan, T.; Fang, J.; Shen, J.; Shi, L.; Zhang, D. Enhanced capacitive deionization of saline water using N-doped rod-like porous carbon derived from dual-ligand metal-organic frameworks. *Environ. Sci.: Nano* **2020**, *7*, 926−937.

(10) Kong, W.; Ge, X.; Zhang, Q.; Wang, Y.; Wang, Y.; Lu, J.; Zhang, M.; Kong, D.; Feng, Y. Ultrahigh content boron and nitrogen

codoped hierarchically porous carbon obtained from biomass byproduct okara for capacitive deionization. *ACS Omega* **2022**, *7*, 48282−48290.
(11) Zornitta, R. L.; Ruotolo, L. A. Simultaneous analysis of electrosorption capacity and kinetics for CDI desalination using different electrode configurations. *Chem. Eng. J.* **2018**, *332*, 33−41.
(12) Leong, Z. Y.; Yang, H. Y. Capacitive deionization of divalent cations for water softening using functionalized carbon electrodes. *ACS Omega* **2020**, *5*, 2097−2106.
(13) Urita, K.; Urita, C.; Fujita, K.; Horio, K.; Yoshida, M.; Moriguchi, I. The ideal porous structure of EDLC carbon electrodes with extremely high capacitance. *Nanoscale* **2017**, *9*, 15643−15649.
(14) Xie, Z.; Shang, X.; Yang, J.; Hu, B.; Nie, P.; Jiang, W.; Liu, J. 3D interconnected boron-and nitrogen-codoped carbon nanosheets decorated with manganese oxides for high-performance capacitive deionization. *Carbon* **2020**, *158*, 184−192.
(15) Han, B.; Cheng, G.; Wang, Y.; Wang, X. Structure and functionality design of novel carbon and faradaic electrode materials for high-performance capacitive deionization. *Chem. Eng. J.* **2019**, *360*, 364−384.
(16) Xiong, Y.; Yang, X.; Liu, Y.; Chen, X.; Wang, G.; Lu, B.; Lin, G.; Huang, B. Fabrication of phosphorus doping porous carbon derived from bagasse for highly-efficient removal of La^{3+} ions via capacitive deionization. *Electrochim. Acta* **2022**, *404*, No. 139735.
(17) Liu, Q.; Wang, N.; Xie, B.; Xiao, D. Improved U(VI) electrosorption performance of hierarchical porous heteroatom-doped electrode based on double-template method. *Sep. Purif. Technol.* **2023**, *308*, No. 122866.
(18) Zeng, J. R.; Chen, L.; Siwal, S.; Zhang, Q. Solvothermal sulfurization in a deep eutectic solvent: a novel route to synthesize Co-doped Ni_3S_2 nanosheets supported on Ni foam as active materials for ultrahigh-performance pseudocapacitors. *Sustainable Energy Fuels* **2019**, *3*, 1957−1965.
(19) Ma, X.; Chen, Y.-A.; Zhou, K.; Wu, P.-C.; Hou, C.-H. Enhanced desalination performance via mixed capacitive-Faradaic ion storage using RuO_2-activated carbon composite electrodes. *Electrochim. Acta* **2019**, *295*, 769−777.
(20) Zhang, B.; Boretti, A.; Castelletto, S. MXene pseudocapacitive electrode material for capacitive deionization. *Chem. Eng. J.* **2022**, *435*, No. 134959.
(21) B, N.; Vidyalakshmi, Y.; Razack, S. A. Enhanced formation of ruthenium oxide nanoparticles through green synthesis for highly efficient supercapacitor applications. *Adv. Powder Technol.* **2020**, *31*, 1001−1006.
(22) Park, S.; Shin, D.; Yeo, T.; Seo, B.; Hwang, H.; Lee, J.; Choi, W. Combustion-driven synthesis route for tunable TiO_2/RuO_2 hybrid composites as high-performance electrode materials for supercapacitors. *Chem. Eng. J.* **2020**, *384*, No. 123269.
(23) Meng, Q.; Xu, W.; Zhu, S.; Liang, Y.; Cui, Z.; Yang, X.; Inoue, A. Low-cost fabrication of amorphous cobalt-iron-boron nanosheets for high-performance asymmetric supercapacitors. *Electrochim. Acta* **2019**, *296*, 198−205.
(24) Allison, A.; Andreas, H. Minimizing the Nyquist-plot semicircle of pseudocapacitive manganese oxides through modification of the oxide-substrate interface resistance. *J. Power Sources* **2019**, *426*, 93−96.
(25) Baran, T.; Wojtyła, S.; Minguzzi, A.; Rondinini, S.; Vertova, A. J. A. C. B. E. Achieving efficient H_2O_2 production by a visible-light absorbing, highly stable photosensitized TiO_2. *Appl. Catal., B* **2019**, *244*, 303−312.
(26) Li, X.; Li, X.; Dong, Y.; Wang, L.; Jin, C.; Zhou, N.; Chen, M.; Dong, Y.; Xie, Z.; Zhang, C. Porous cobalt oxides/carbon foam hybrid materials for high supercapacitive performance. *J. Colloid Interface Sci.* **2019**, *542*, 102−111.
(27) Chen, Y.; Liu, T.; Zhang, L.; Yu, J. N-doped graphene framework supported nickel cobalt oxide as supercapacitor electrode with enhanced performance. *Appl. Surf. Sci.* **2019**, *484*, 135−143.
(28) Geuli, O.; Hao, Q.; Mandler, D. One-step fabrication of NiOx-decorated carbon nanotubes-$NiCo_2O_4$ as an advanced electroactive composite for supercapacitors. *Electrochim. Acta* **2019**, *318*, 51−60.
(29) Shi, S.; Wan, G.; Wu, L.; He, Z.; Wang, K.; Tang, Y.; Xu, X.; Wang, G. Ultrathin manganese oxide nanosheets uniformly coating on carbon nanocoils as high-performance asymmetric supercapacitor electrodes. *J. Colloid Interface Sci.* **2019**, *537*, 142−150.
(30) Bi, T.; Fang, H.; Jiang, J.; He, X.; Zhen, X.; Yang, H.; Wei, Z.; Jia, Z. Enhance supercapacitive performance of MnO_2/3D carbon nanotubes-graphene as a binder-free electrode. *J. Alloys Compd.* **2019**, *787*, 759−766.
(31) Xiang, C.; Li, M.; Zhi, M.; Manivannan, A.; Wu, N. A reduced graphene oxide/Co_3O_4 composite for supercapacitor electrode. *J. Power Sources* **2013**, *226*, 65−70.
(32) Qi, Z.; Younis, A.; Chu, D.; Li, S. A facile and template-free one-pot synthesis of Mn_3O_4 nanostructures as electrochemical supercapacitors. *Nano-Micro Lett.* **2016**, *8*, 165−173.
(33) Sahoo, R.; Pham, D. T.; Lee, T. H.; Luu, T. H. T.; Seok, J.; Lee, Y. H. Redox-driven route for widening voltage window in asymmetric supercapacitor. *ACS Nano* **2018**, *12*, 8494−8505.
(34) Ding, Y.; Dai, L.; Wang, R.; Wang, H.; Zhang, H.; Jiang, W.; Tang, J.; Zang, S.-Q. Bio-inspired Mn_3O_4@ N, P-doped carbon cathode for 2.6 V flexible aqueous asymmetric supercapacitors. *Chem. Eng. J.* **2021**, *407*, No. 126874.
(35) Chang, W. T.; Chen, P.-A.; Peng, C.-Y.; Liu, S.-H.; Wang, H. P. Capacitive deionization and disinfection of saltwater using nanostructured (Cu-Ag)@C/rGO composite electrodes. *Environ. Sci.: Water Res. Technol.* **2023**, *9*, 883−889.
(36) Huang, C.-H.; Wang, H. P.; Chang, J.-E.; Eyring, E. M. Synthesis of nanosize-controllable copper and its alloys in carbon shells. *Chem. Commun.* **2009**, *31*, 4663−4665.
(37) Tholkappiyan, R.; Naveen, A. N.; Vishista, K.; Hamed, F. Investigation on the electrochemical performance of hausmannite Mn_3O_4 nanoparticles by ultrasonic irradiation assisted co-precipitation method for supercapacitor electrodes. *J. Taibah Univ. Sci.* **2018**, *12*, 669−677.
(38) Kim, K. S.; Park, Y. J. Catalytic properties of Co_3O_4 nanoparticles for rechargeable Li/air batteries. *Nanoscale Res. Lett.* **2012**, *7*, No. 47.
(39) Lu, T.; Chen, Q. A simple method of identifying π orbitals for non-planar systems and a protocol of studying π electronic structure. *Theor. Chem. Acc.* **2020**, *139*, 25.
(40) Chen, N.; Wang, D.; Hu, J.; Guan, L.; Lu, Z.-H. Measuring energy gaps of organic semiconductors by electron energy loss spectroscopies. *Phys. Status Solidi B* **2022**, *259*, No. 2100459.
(41) Hou, C.-C.; Ma, C.; Zhang, S.-N.; Wang, L.-Y.; Wang, K.-X.; Chen, J.-S. Polymeric Schiff Base with Thiophene Rings for Sodium-Ion Batteries. *ACS Appl. Energy Mater.* **2022**, *5*, 13802−13807.
(42) Li, X.; Xiang, Z. Identifying the impact of the covalent-bonded carbon matrix to FeN4 sites for acidic oxygen reduction. *Nat. Commun.* **2022**, *13*, No. 57.
(43) Abraham, J. P.; Sajan, D.; Shettigar, V.; Dharmaprakash, S.; Němec, I.; Joe, I. H.; Jayakumar, V. Efficient π-electron conjugated push−pull nonlinear optical chromophore 1-(4-methoxyphenyl)-3-(3, 4-dimethoxyphenyl)-2-propen-1-one: A vibrational spectral study. *J. Mol. Struct.* **2009**, *917*, 27−36.
(44) Ning, J.; Xia, M.; Wang, D.; Feng, X.; Zhou, H.; Zhang, J.; Hao, Y. Superior pseudocapacitive storage of a novel Ni_3Si_2/NiOOH/graphene nanostructure for an all-solid-state supercapacitor. *Nano-Micro Lett.* **2021**, *13*, 2.
(45) Ko, J. S.; Sassin, M. B.; Parker, J. F.; Rolison, D. R.; Long, J. W. Combining battery-like and pseudocapacitive charge storage in 3D MnO_x@ carbon electrode architectures for zinc-ion cells. *Sustainable Energy Fuels* **2018**, *2*, 626−636.
(46) Wang, L.; Liu, X.; Wang, X.; Yang, X.; Lu, L. Electrochemical capacitance study on Co $_3O_4$ nanowires for super capacitors application. *J. Mater. Sci.: Mater. Electron.* **2011**, *22*, 601−606.
(47) Zhao, N.; Fan, H.; Zhang, M.; Ma, J.; Wang, C.; Yadav, A. K.; Li, H.; Jiang, X.; Cao, X. Beyond intercalation-based supercapacitors:

https://doi.org/10.1021/acsomega.3c00673
ACS Omega 2023, 8, 13315−13322

The electrochemical oxidation from Mn_3O_4 to $Li_4Mn_5O_{12}$ in Li_2SO_4 electrolyte. *Nano Energy* **2020**, *71*, No. 104626.
(48) Bharath, G.; Arora, N.; Hai, A.; Banat, F.; Savariraj, D.; Taher, H.; Mangalaraja, R. Synthesis of hierarchical Mn_3O_4 nanowires on reduced graphene oxide nanoarchitecture as effective pseudocapacitive electrodes for capacitive desalination application. *Electrochim. Acta* **2020**, *337*, No. 135668.
(49) Younes, H.; Ravaux, F.; El Hadri, N.; Zou, L. Nanostructuring of pseudocapacitive $MnFe_2O_4$/Porous rGO electrodes in capacitive deionization. *Electrochim. Acta* **2019**, *306*, 1−8.
(50) Younes, H.; Zou, L. Asymmetric configuration of pseudocapacitive composite and rGO electrodes for enhanced capacitive deionization. *Environ. Sci.: Water Res. Technol.* **2020**, *6*, 392−403.

https://doi.org/10.1021/acsomega.3c00673
ACS Omega 2023, 8, 13315−13322